Mode engineering in reconfigurable fractal topological circuits

Jiajun He,[1] Hao Jia,[1,*] Haoxiang Chen,[1] Tao Wang,[1] Shuo Liu,[2] Jianjun Cao,[3] Zhen Gao,[4] Ce Shang,[5,6,†] and Tie Jun Cui[2,‡]

[1]*School of Physical Science and Technology, Lanzhou University, Lanzhou 730000, China*
[2]*State Key Laboratory of Millimeter Waves, Southeast University, Nanjing 210096, China*
[3]*School of Science, Jiangnan University, Wuxi 214122, China*
[4]*Department of Electronic and Electrical Engineering, Southern University of Science and Technology, Shenzhen 518055, China*
[5]*Aerospace Information Research Institute, Chinese Academy of Sciences, Beijing 100094, China*
[6]*Physical Science and Engineering Division, King Abdullah University of Science and Technology, Thuwal 23955-6900, Saudi Arabia*

(Received 1 March 2024; revised 25 April 2024; accepted 23 May 2024; published 6 June 2024)

Circuits can provide a versatile platform for exploring new physics, particularly in probing the topological phases within complex geometries. Fractals, celebrated for their intricate, self-similar duality, and noninteger dimensions, particularly those embedded in complex manifolds, remain uncharted in this context. In our research, we implement Sierpiński fractal topological insulators within reconfigurable fractal topological circuits while expanding the scope to include the cylindrical and toroidal structures. Our approach is grounded in consistency theory and reinforced through experimental verification, confirming the presence of unconventional higher-order topological phenomena referring to the abundance of topological edge and corner modes. Intriguingly, the quantity of these edge and corner modes is proportional to the volume modes relative to the system size, with an exponent aligning with the Hausdorff fractal dimension of the Sierpiński carpet. This study paves the way for a deeper exploration of topological modes within fractal geometries, potentially unlocking new avenues in topological physics.

DOI: 10.1103/PhysRevB.109.235406

I. INTRODUCTION

Topological insulators are a special class of materials that have a nontrivial topology in the bulk band structure and exhibit topologically protected edge modes at the boundary [1–4]. High-order topological insulators (HOTIs) are a new class of topological insulators with dimensions $d > 1$ [5–9]. These higher-order topological insulators possess $(d-1)$-dimensional boundaries that, unlike conventional topological insulators, do not conduct through gapless modes but, instead, are themselves topological insulators. An increasing number of systems are being used to model topological phenomena in electronic systems, including ultracold quantum gases [10–15] and photonic [16–25], acoustic [8,26–33], mechanical [34–38], and electrical circuit systems [39–50]. Among them, circuit systems composed of inductors and capacitors are particularly notable for their flexibility in design, ease of implementation, and integration [39,40]. Circuits facilitate designs by incorporating various types of components and enable the realization of nonlinear [47,48], non-Abelian [43], and non-Hermitian modes [45,50,51], which are challenging to achieve in alternative systems.

Fractal geometry, rooted in recursive mathematical iterations, manifests diverse physics due to intricate and repeating patterns and is emerging as a promising prototype for systems embodying noninteger dimensions. Fractals, especially those grounded in higher-order topological insulators, have seen significant advances in understanding topological physics in noninteger dimensions in the fields of photonics and acoustics [17,29]. However, photonic and acoustic systems often lack the crucial aspect of reconfigurability. In modern electronic design, reconfigurability empowers a circuit with multifunctional capabilities. This feature is especially pronounced in reconfigurable fractal topological circuits (RFTCs), allowing adaptation to various operational modes. The "mode" refers to a circuit's specific operational state, influenced by frequency response, impedance, and current flow. Mode engineering in RFTCs is a critical process, involving the strategic manipulation of these modes to achieve desired functionalities. Our work delves into the theoretical and experimental intricacies, demonstrating how RFTCs can yield versatile electronic behaviors.

To develop RFTCs, we employ a modular approach to two-dimensional (2D) Su-Schrieffer-Heeger (SSH) circuits, selectively deactivating specific regions to design Sierpiński fractal configurations. Compared to conventional 2D SSH circuits, we observe that square Sierpiński carpets exhibit a higher count of corner and edge modes. To further enhance the reconfigurability of these systems, we introduce fully controllable boundary conditions by selectively tailoring the circuit connections among different nodes and are able to embed RFTCs in cylindrical and toroidal geometries. The aggregate of these modes rivals the number of topological

*jiahao@lzu.edu.cn
†shang.ce@kaust.edu.sa
‡tjcui@seu.edu.cn

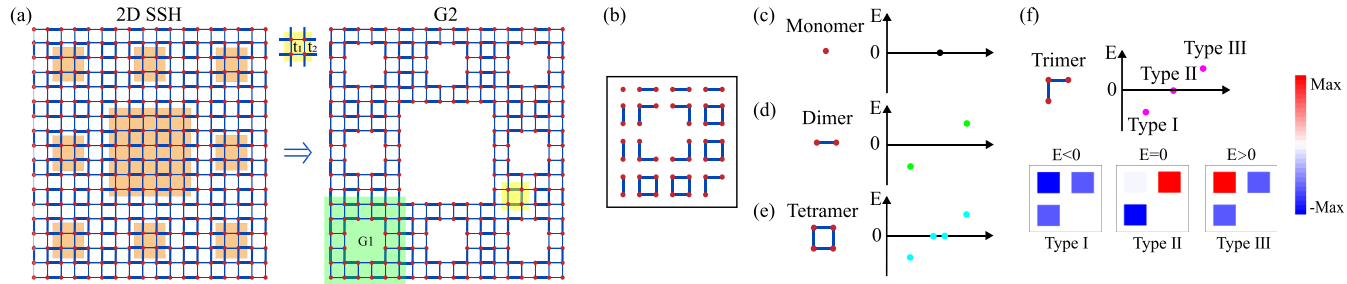

FIG. 1. Evolution from the 2D SSH model to the fractal higher-order topological model. (a) Constructing square Sierpiński carpets from the 2D SSH model. The yellow box indicates the unit cell, and the orange box indicates the central square that should be removed. The green box indicates the first-generation Sierpiński carpet G(1) which is formed by removing the central square. (b) Decomposition of the G(2) Sierpiński fractal topological tight-binding model with $t_1 = 0$, which is constituted by monomers, dimers, trimers, and tetramers. (c) Monomers at the outer corner boundaries. Each monomer supports a zero-energy outer corner mode. (d) Dimers at the inner and outer edge boundaries. Each dimer supports a bonding edge mode and an antibonding edge mode. (e) Tetramers in the bulk. Each tetramer supports a negative-energy, a positive-energy, and two zero-energy bulk modes. (f) Trimmers in the inner corners and the energy distribution. Each trimer supports three inner corner modes with negative (type I), zero (type II), and positive (type III) energy states.

modes, suggesting that the corners, edges, and bulk within these fractals possess different properties for different geometries, leading to specific design rules for mode engineering. Such an approach not only broadens the scope of reconfigurability but also provides a versatile framework for exploring novel topological phenomena in complex geometrical settings.

II. RESULTS

We undertake the theoretical analysis by implementing the fractal higher-order topological modes based on the 2D SSH model. The conventional 2D SSH model has four sites and fourfold rotation symmetry in each unit cell, with intercell couplings t_2 being stronger than intracell couplings t_1. To realize fractal higher-order topological modes, we tailor the structure to construct square Sierpiński carpets, as shown in Fig. 1(a). The first-generation Sierpiński carpet G(1) is formed by removing the central square of the green region, and the second-generation Sierpiński carpet G(2) is formed by dividing a square into nine smaller squares and removing the central square. Thus, to generalize, the Nth-generation Sierpiński carpet G(n) is achieved by recursively applying this process to the remaining squares for each subsequent generation. Different iterations of Sierpiński carpets all have the same Hausdorff fractal dimension,

$$d_f = \ln(8)/\ln(3) \approx 1.893. \tag{1}$$

To further analyze the scaling characteristics of the number of corner, edge, and bulk modes, we tune the weak coupling coefficient t_1 to zero. In this case, the Sierpiński carpet consists of four types of structural elements, namely, monomers, dimers, trimers, and tetramers [Fig. 1(b)], each supporting different local orbits. This adiabatic process ensures the preservation of topological invariants and provides a way to directly compute the corner, edge, and bulk modes. Among these structural elements, monomers appear at the outer corner boundary and support a zero-energy outer corner mode [Fig. 1(c)]. Dimers appear at the inner and outer edge boundaries, facilitating edge modes on the boundaries and supporting bonding and antibonding modes, thus forming two edge spectral continua above and below zero energy, respectively [Fig. 1(d)]. The tetramers come from the bulk position and have four eigenstates with positive, negative, and zero energies [Fig. 1(e)], forming a three-bulk spectral continuum. Trimers stem from the inner corner boundary and support three local orbitals. They have a negative-energy orbital (type I), a zero-energy orbital (type II), and a positive-energy orbital [type III; Fig. 1(f)]. The inner corner modes of types I and III are symmetric eigenstates, while the inner corner modes of type II are antisymmetric. The emergence of inner corner modes can be considered a distinctive feature of fractal HOTIs. Based on the analysis, the numbers of monomers, dimers, trimers, and tetramers are determined as follows:

$$N_1(n) = 4, \quad N_2(n) = \frac{16}{5} \times 3^n + \frac{1}{35} \times 8^{n+1} - \frac{24}{7}, \tag{2}$$

$$N_3(n) = \frac{4 \times (8^n - 1)}{7},$$

$$N_4(n) = \frac{8}{7} - \frac{8}{5} \times 3^n + \frac{16}{35} \times 8^n \tag{3}$$

for the G(n) ($n = 1, 2, 3, \ldots$) Sierpiński carpet, and the number of outer corner modes, edge modes, inner corner modes, and bulk modes are $N_{oc} = N_1, N_{ed} = 2N_2, N_{ic} = 3N_3$, and $N_{bk} = 4N_4$. The total numbers satisfy the sum rule:

$$N_{oc} + N_{ed} + N_{ic} + N_{bk} = 4 \times 8^n. \tag{4}$$

For instance, for G(2) in Fig. 1(a), 256 eigenmodes exist; among them, there are 64 bulk modes, 80 edge modes, and 112 corner modes.

We further transform the planar Sierpiński carpet into cylindrical and toroidal topological models by selectively configuring the boundaries of the circuits. When the sites along the x or y boundaries are connected, the cylindrical topological model can be realized as in Fig. 2(b), while the toroidal topological model can be achieved by simultaneously connecting the x and y boundaries, as shown in Fig. 2(c). For the cylindrical topological model, using the same analysis method as that

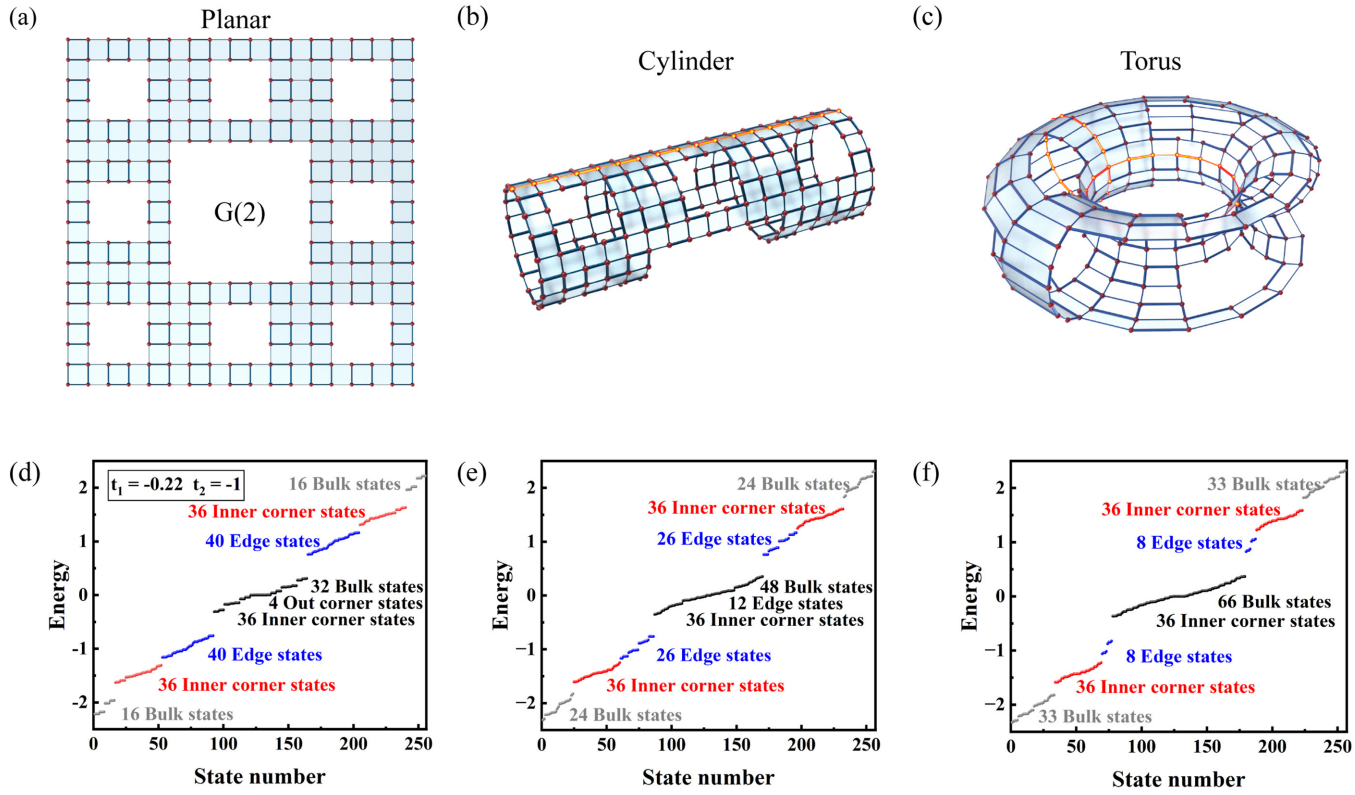

FIG. 2. Geometric topology and eigenstate spectra of the Sierpiński fractal higher-order topological model, cylindrical topological model, and toroidal topological model. (a) Second-order Sierpiński fractal topological model G(2). (b) Cylindrical topological model. (c) Toroidal topological model. (d) Eigenstate spectrum of the G(2) Sierpiński fractal topological model. (e) Eigenstate spectrum of the cylindrical topological model. (f) Eigenstate spectrum of the toroidal topological model.

for the Sierpiński carpet, the numbers of monomers, dimers, trimers, and tetramers are derived as follows:

$$N_1 = 0, \quad N_2 = \frac{6}{5} \times 3^n + \frac{1}{35} \times 8^{n+1} + \frac{4}{7}, \tag{5}$$

$$N_3 = \frac{4 \times (8^n - 1)}{7},$$

$$N_4 = -\frac{3}{5} \times 3^n + \frac{2}{35} \times 8^{n+1} + \frac{1}{7}. \tag{6}$$

For the toroidal topological geometry, the quantities of monomers, dimers, trimers, and tetramers are calculated as follows:

$$N_1 = 0, \quad N_2 = -\frac{4}{5} \times 3^n + \frac{1}{35} \times 8^{n+1} + \frac{4}{7}, \tag{7}$$

$$N_3 = \frac{4 \times (8^n - 1)}{7},$$

$$N_4 = \frac{2}{5} \times 3^n + \frac{2}{35} \times 8^{n+1} + \frac{1}{7}. \tag{8}$$

With the formulas above, the numbers of outer corner modes, edge modes, inner corner modes, and bulk modes can be calculated like those in the planar scenario. Specifically, we analyze the detailed eigenstates, for instance, G(2) with $t_1 = -0.22$ and $t_2 = -1$. The eigenstate spectra for the G(2) Sierpiński fractal higher-order topological model, the cylindrical model, and the toroidal topological model are shown in Figs. 2(d), 2(e), and 2(f), respectively.

It can be observed that the total number of eigenstates remains constant in the three cases, which is decided by Eq. (4). For instance, Sierpiński carpet G(2) is 256. However, the number of bulk, edge, and corner modes in the cylindrical and toroidal topological models is engineered. As shown in Fig. 2(d), there are 64 bulk modes, 80 edge modes, and 112 corner modes in the planar Sierpiński carpet. There is a high number of edge and corner modes, which is a major feature of the topological mode of fractals due to the abundance of edge and corner boundaries in fractal geometries. From the eigenstate spectrum [Figs. 2(e) and 2(f)], there are 96 bulk modes, 52 edge modes, and 108 corner modes in the cylindrical model and 132 bulk modes, 16 edge modes, and 108 corner modes in the toroidal model. Compared to those of planar Sierpiński carpets, the eigenstates are significantly modulated. There is no outer corner mode in either the cylindrical and or toroidal model. The outer corner mode and partial edge mode in the cylindrical model are transformed into the bulk mode, but the number of inner corner modes remains constant. Compared to the cylindrical model, the remaining number of edge modes decreases further, and the vanishing ones are turned into bulk modes. During this procedure, the number of inner corner

modes remains unchanged:

$$\begin{bmatrix} i\omega(2C_1+2C_2)+\frac{1}{i\omega L} & -i\omega C_1 & 0 & \cdots & 0 & -i\omega C_1 & \cdots \\ -i\omega C_1 & i\omega(2C_1+2C_2)+\frac{1}{i\omega L} & -i\omega C_1 & \cdots & 0 & 0 & \cdots \\ 0 & -i\omega C_2 & i\omega(2C_1+2C_2)+\frac{1}{i\omega L} & \cdots & 0 & 0 & \cdots \\ \vdots & \vdots & & \ddots & \vdots & \vdots & \\ 0 & 0 & 0 & \cdots & i\omega(2C_1+2C_2)+\frac{1}{i\omega L} & 0 & \cdots \\ -i\omega C_1 & 0 & 0 & \cdots & 0 & i\omega(2C_1+2C_2)+\frac{1}{i\omega L} & \cdots \\ \vdots & \vdots & \vdots & & \vdots & \vdots & \ddots \end{bmatrix}. \tag{9}$$

In the following, we validate the theoretical analysis by constructing a proof of concept on a topological circuit platform. With the elaborately designed RFTCs, we can observe the different characteristics on identical printed circuit boards (PCBs). The coupling coefficients t_1 and t_2 in the fundamental 2D SSH model are built from capacitors C_1 and C_2 with capacitance values of 0.22 and 1 nF, so the hopping ratio $t := t_1/t_2 = C_1/C_2 = 0.22 < 1$. Identical inductors L with an inductance value of 440μH are connected between each site and a common isolated grounding plate. The Laplacian J for the circuit is given by Eq. (9).

At the center frequency, we have

$$i\omega(2C_1+2C_2)+\frac{1}{i\omega L}=0, \tag{10}$$

so the relationship between J and the H is

$$J = i\omega M_0 H, \tag{11}$$

where H is the Hamiltonian of the topological system,

$$\begin{bmatrix} 0 & t_1 & 0 & \cdots & 0 & t_1 & 0 & \cdots \\ t_1 & 0 & t_2 & \cdots & 0 & 0 & t_1 & \cdots \\ 0 & t_2 & 0 & \cdots & 0 & 0 & 0 & \cdots \\ \vdots & \vdots & & \ddots & & \vdots & \vdots & \\ 0 & 0 & 0 & \cdots & 0 & 0 & 0 & \cdots \\ t_1 & 0 & 0 & \cdots & 0 & 0 & t_1 & \cdots \\ 0 & t_1 & 0 & \cdots & 0 & t_1 & 0 & \cdots \\ \vdots & \vdots & \vdots & & \vdots & \vdots & \vdots & \ddots \end{bmatrix}, \tag{12}$$

and $M_0 = -C_i/t_i$, $(i = 1, 2)$ is the multiplication coefficient that shows the ratio of the circuit capacitance and coupling coefficient. The whole circuit contains 324 sites and is constructed on an 18×18 matrix, which corresponds to the arrangement in Fig. 1(a). Figure 3(a) illustrates the whole electric connection, and the representative site locations that are used to characterize the outer corner, edge, and bulk modes are marked with red, green, and blue rectangles. At the boundaries of the nine smaller squares, single-pole double-throw (SPDT) switches are set up to toggle the connections between the next-neighbor site and grounding plate with compensating boundary conditions. In this way, the circuits in nine squares can be selectively removed from the system; thus, the remaining number of sites is 256, and the circuit topology evolves into Sierpiński carpet G(2). The corresponding circuit is illustrated in Fig. 3(b). To facilitate the analysis, we also classify all positions of sites in the circuit into four different types, those located in the bulk region (tetramers), the edge region (dimers), the inner corner region (trimers), and the outer corner region (monomers). The representative site locations that are used to characterize the outer corner, edge, inner corner A, inner corner B, and bulk modes are marked with green, orange, blue, purple, and gray rectangles. To realize the cylindrical and toroidal models, we set up one-by-one pin headers that connect each site located along the x and y boundaries. When the pin headers in one or two directions are connected, the corresponding geometries are achieved.

We use LTSPICE to simulate and analyze the circuits with the central frequency at $f_0 = [2\pi\sqrt{LC}]^{-1} \approx 153$ kHz. The impedance spectra at representative sites are scanned from 100 to 250 kHz (i.e., $0.65\omega_0$–$1.63\omega_0$), as illustrated in Figs. 3(c) and 3(d). When the impedance spectra are carefully examined, we can find the frequency related to the corresponding eigenmodes. It can be observed that the impedance spectrum of the outer corner mode (the green curve) has one peak at a frequency of 153.49 kHz, and the impedance spectrum of the edge mode (the orange curve) has two peaks at frequencies of 127.91 and 204.98 kHz. The bulk mode spectrum (the gray line) has three peaks at frequencies of 110.51, 153.2, and 228.02 kHz. We select the frequency peak corresponding to each impedance spectrum and get the impedance distribution of whole circuit sites in the 2D SSH model and Sierpiński carpet G(2). The intensities of the spectra are normalized to their relative values and plotted in Figs. 3(c) and 3(d) with frame colors identical to the related curves for the impedance spectra. It should be noted that the inner corner modes can be classified into three types: types I and III are symmetric, and type II is antisymmetric. The impedance spectrum of inner corner mode A (blue line) has three peaks located at frequencies of 119.16, 154.91, and 249.77 kHz, while the impedance curve of inner corner mode B (purple line) has two peaks at frequencies of 121.35 and 237.95 kHz; the peak corresponding to the type II trimer vanishes due to location symmetry. The impedance distributions for inner corner mode A and inner corner mode B represent two different states of the energy distribution, as shown on the right in Fig. 3(d). By comparing the experimentally measured

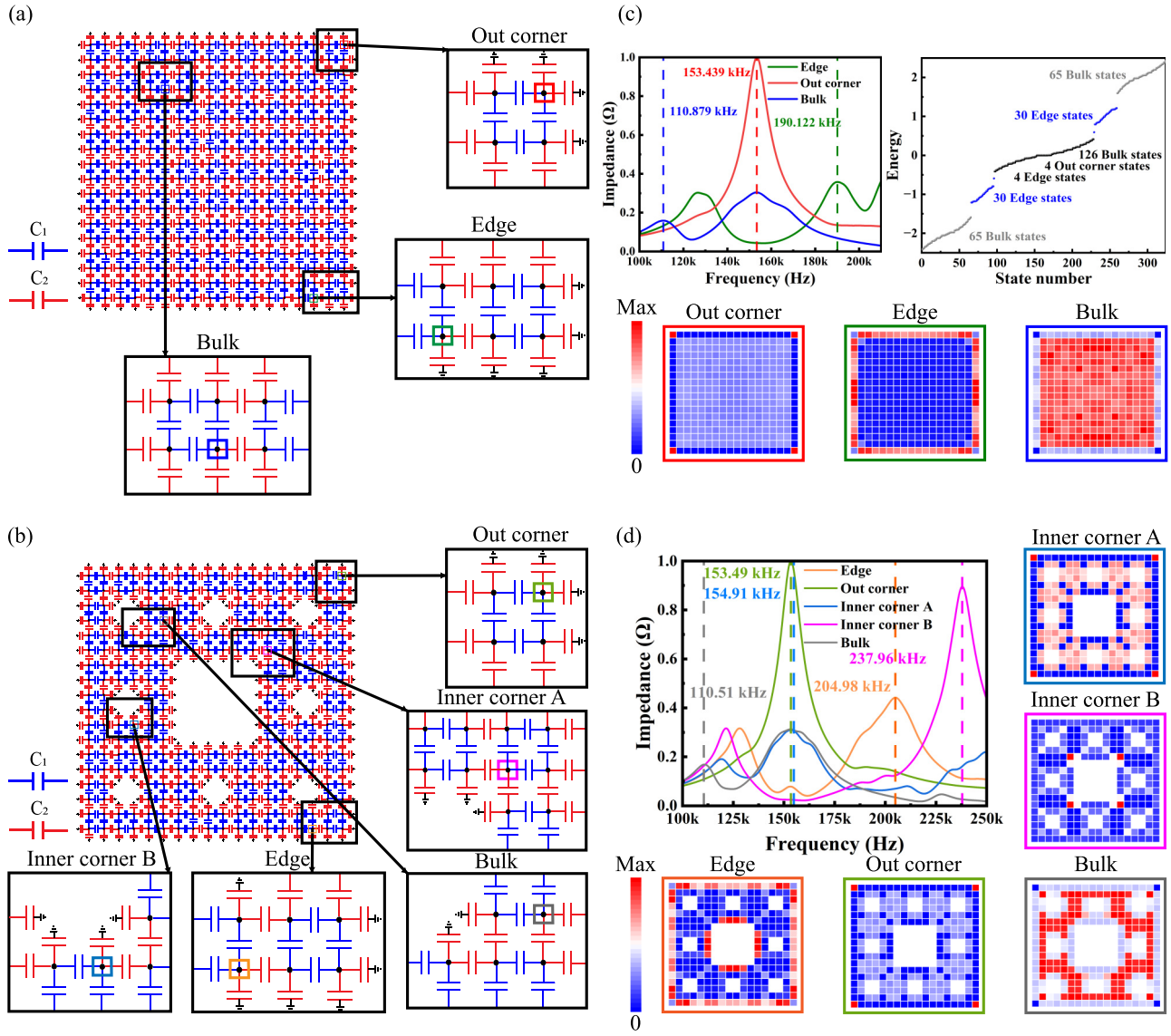

FIG. 3. Circuit realization and simulation results for the 2D SSH model and the Sierpiński carpet G(2) model. (a) The circuit implementation of the 2D SSH model. $C_1 = 0.22$ nF, $C_2 = 1$ nF, and $L = 440$ μH. Red, green, and gray rectangles in the magnified local areas indicate the representative sites in the outer corner, edge, and bulk region. For clarity, the grounded inductors are not shown in the circuit. (b) The circuit implementation of the Sierpiński carpet circuit G(2) model. Green, blue, purple, gray, and brown rectangles in the magnified local areas indicate representative sites in the outer corner, edge, inner corner A, inner corner B, and bulk region. (c) Simulated impedance spectrum for three representative sites, the eigenstate spectrum, and the entire impedance distribution of the outer corner mode (red frame), the edge mode (green frame), and the bulk mode (gray frame) for the 2D SSH model. (d) Simulated impedance spectrum for five representative sites and the impedance distribution of the edge modes (brown frame), outer corner modes (green frame), type II inner corner modes (blue frame), type III inner corner modes (purple frame), and bulk modes (gray frame) for the Sierpiński carpet G(2) model.

impedance distribution in Fig. 3(d) with the localized distribution shown in Fig. 1(f), we can clearly distinguish that the type II inner corner A is symmetric and type III inner corner B is antisymmetric. Overall, compared to the 2D SSH model, due to the presence of the inner corner and inner edges, the impedance distribution of the Sierpiński carpet G(2) presents several unique characteristics: the bulk mode is no longer uniform, but the inner edge is also presented as the edge mode. For the 2D SSH model, the corner modes are all bound state in the continuum (BIC) modes [52]. However, there are two different types of corner modes in the Sierpiński fractal lattice. According to the eigenstate spectrum of the G(2) Sierpiński fractal model, the outer corner modes and the inner corner modes corresponding to the black dots are also BIC modes, and they have the same characteristics as those in the 2D SSH model [53]. The inner corner modes corresponding to the pink squares are in-gap topological modes; they are stable and exhibit much higher robustness due to the topological protection.

Based on the simulation results, we perform the experimental verification. The circuit layout is implemented on an FR-4 PCB. Capacitors C_1 and C_2 are multilayer ceramic capacitors with capacitances of 0.21 and 1 nF. The inductors are chosen with an inductance value of 0.44 mH. The

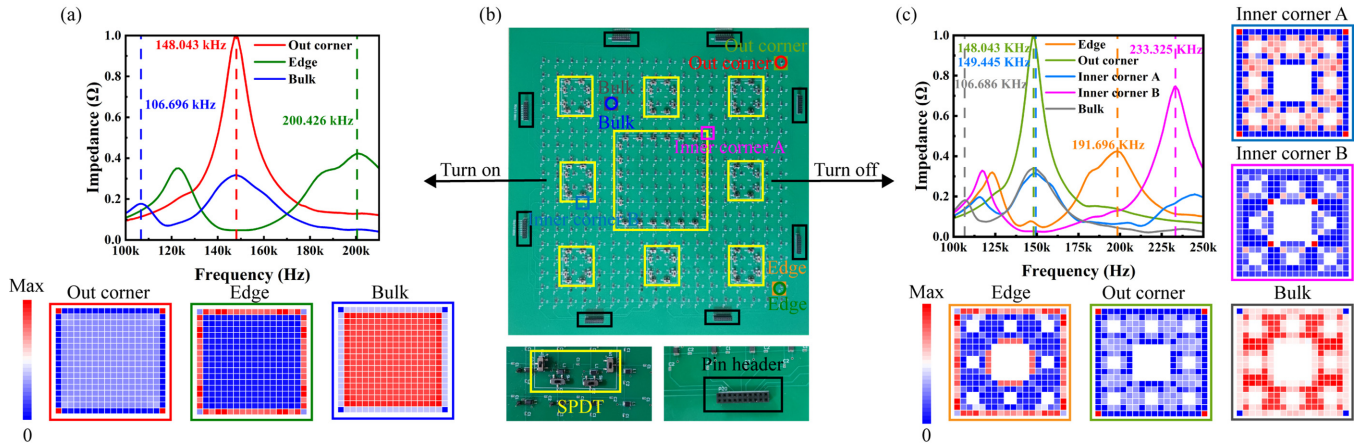

FIG. 4. Circuit experimental realization of the 2D SSH model and Sierpiński carpet G(2). (a) Experimentally measured impedance spectra of the outer corner, edge, bulk modes, and the impedance distributions corresponding to the outer corner mode (red frame), edge mode (green frame), and bulk mode (blue frame) for the 2D SSH model. (b) PCB layout of the RFTC and designed switches for reconfiguration functionality in magnified areas. The yellow rectangles indicate the single-pole double-throw (SPDT) switch, and the black rectangles indicate the pin header connectors. (c) Experimentally measured impedance spectra of the edge, outer corner, inner corner A, inner corner B, and bulk modes and the impedance distribution corresponding to the edge mode (brown frame), outer corner mode (green frame), inner corner mode A (blue frame), inner corner mode B (purple frame), and bulk mode (gray frame).

fabricated test board is illustrated in Fig. 4(b). SPDT switches are located at the boundary of the subsquare that should be reconfigured in the Sierpiński carpet and indicated by the yellow rectangle. We use the switch manipulation descriptions "turned on" and "turned off" to indicate whether the components in subsquares are connected to the circuit system or not. Female pin headers, indicated by the black box, are connected to all the sites located in the x and y boundaries. When they are grounded (default connection), we have the normal planar Sierpiński carpet. If we connect the pin headers along one boundary direction (either horizontal or vertical), it evolves into the cylinder. By connecting the pin headers along both orthogonal directions, it becomes a torus.

First, we configure the pin headers so that the circuits are planar. By toggling the state of the SPDT switches between turned on and turned off, we use the impedance analyzer to inspect the impedance spectra and impedance distributions in both the 2D SSH model and Sierpiński carpet G(2); the results are shown in Figs. 4(a) and 4(c), respectively. According to the simulation results, the center frequency of the circuit is approximately 154 kHz, so the frequency sweep range is selected to be from 100 to 250 kHz. To facilitate a comparison, the impedance spectra are measured from representative sites identical to those used in the simulation. For the 2D SSH model, the measured impedance peaks are located in the outer corner mode (148.043 kHz), edge mode (200.426 kHz), and bulk mode (106.696 kHz). For the Sierpiński carpet, the measured impedance peaks are distributed in the outer corner mode (148.043 kHz), inner corner modes (149.445 and 244.702 kHz), edge mode (191.696 kHz), and bulk mode (106.686 kHz). The experimental impedance spectra and impedance distributions strongly match the simulation results, elucidating the effectiveness of our analysis and experiment. The small frequency peak drift between the simulation and experimental results mainly comes from the peak expansion in spectra due to the parasitic parameters of the capacitors and inductors and the impedance value fluctuation among different elements.

In the following, we keep the state of the SPDT switches in the turned off state and configure the connection of pin headers, so that the circuits are transformed to cylindrical and toroidal geometries. To provide a more intuitive vision for comparison, we demonstrate the simulation and experimental results for representative impedance distribution simultaneously in Figs. 5(a) and 5(b). The geometry changes in topology cause the mode of mutual transformation. The outer corner modes vanish, and the distribution states of the edge and bulk modes are influenced. According to Fig. 5(a), the outer corner modes are transformed to the edge modes in the cylindrical geometry. At the frequency of the original edge mode, it can be observed that the edge modes appear along only one direction and the edge modes along the orthogonal direction do not exist, which matches the geometry characteristics well. Similarly, according to Fig. 5(b), the outer corner modes turn into bulk modes. Moreover, some of the original edge modes are transformed into bulk modes, as the original edges in two directions are combined. However, the geometry transformation does not influence the environment of the inner corner mode and inner edge modes, so their distribution remains constant. As a result, the number of edge modes decreases, and the bulk modes increase further. The experimental results are consistent with the simulation results, which shows the precision of this method. The observed results also match Fig. 2(e) well, indicating the capability of engineering the number of topological modes through RFTCs.

III. CONCLUSION

In conclusion, we presented RFTCs for the exploration of fractal geometry. By selectively deactivating specific regions or connecting certain boundaries within the 2D SSH circuit, we successfully manifested the planar square Sierpiński carpet and the corresponding cylindrical and toroidal models.

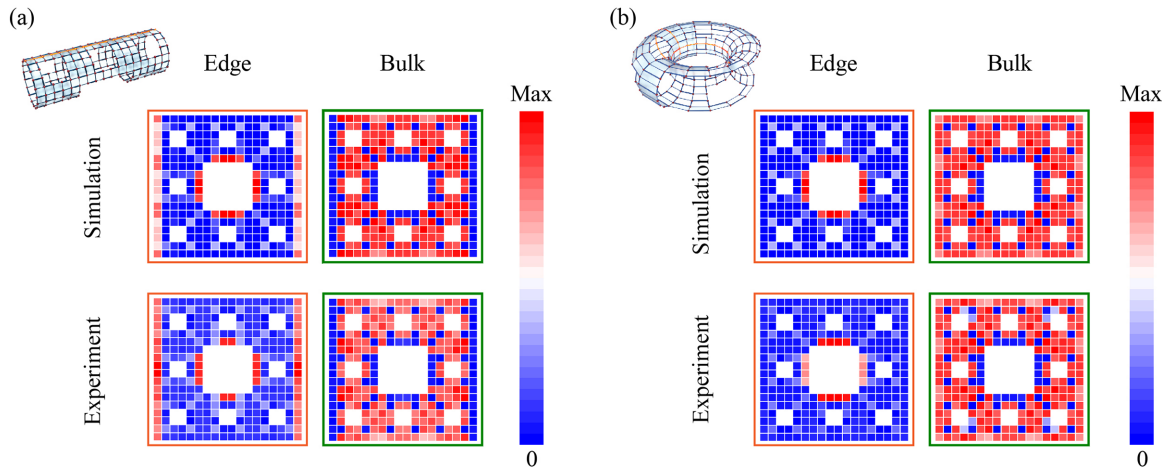

FIG. 5. The simulation and experimental result for the cylindrical and toroidal Sierpiński fractal circuit G(2). (a) Impedance distribution of the cylindrical Sierpiński fractal circuit. (b) Impedance distribution of the toroidal Sierpiński fractal circuit.

Our theoretical analysis, simulations, and experimental results demonstrate a high degree of consistency. In comparison to conventional HOTIs, fractal HOTIs exhibit enhanced richness in edge and corner modes. The cylindrical and toroidal geometries further transform the outer corner and edge modes into bulk modes, suggesting that the corners, edges, and bulk within these fractals can be engendered by different geometries. Our work establishes promising design principles for mode engineering. This innovative approach not only expands the realm of reconfigurability but also offers a versatile framework for investigating emerging topological phenomena in complex geometric scenarios in the future.

ACKNOWLEDGMENTS

We acknowledges funding for this work from the National Key Research and Development Program of China under Grant No. 2022YFA1404903 and the National Natural Science Foundation of China under Grants No. 61905101 and No. 62288101.

[1] M. Z. Hasan and C. L. Kane, Rev. Mod. Phys. **82**, 3045 (2010).
[2] D. Xiao, M.-C. Chang, and Q. Niu, Rev. Mod. Phys. **82**, 1959 (2010).
[3] X.-L. Qi and S.-C. Zhang, Rev. Mod. Phys. **83**, 1057 (2011).
[4] A. Bansil, H. Lin, and T. Das, Rev. Mod. Phys. **88**, 021004 (2016).
[5] F. Schindler, A. M. Cook, M. G. Vergniory, Z. Wang, S. S. P. Parkin, B. A. Bernevig, and T. Neupert, Sci. Adv. **4**, eaat0346 (2018).
[6] A. Dutt, M. Minkov, I. A. Williamson, and S. Fan, Light Sci. Appl. **9**, 131 (2020).
[7] I. Petrides and O. Zilberberg, Phys. Rev. Res. **2**, 022049(R) (2020).
[8] H. Xue, Y. Yang, G. Liu, F. Gao, Y. Chong, and B. Zhang, Phys. Rev. Lett. **122**, 244301 (2019).
[9] F. Schindler, Z. Wang, M. G. Vergniory, A. M. Cook, A. Murani, S. Sengupta, A. Y. Kasumov, R. Deblock, S. Jeon, I. Drozdov, H. Bouchiat, S. Guéron, A. Yazdani, B. A. Bernevig, and T. Neupert, Nat. Phys. **14**, 918 (2018).
[10] N. R. Cooper, J. Dalibard, and I. B. Spielman, Rev. Mod. Phys. **91**, 015005 (2019).
[11] D.-W. Zhang, Y.-Q. Zhu, Y. Zhao, H. Yan, and S.-L. Zhu, Adv. Phys. **67**, 253 (2018).
[12] K. Wintersperger, C. Braun, F. N. Ünal, A. Eckardt, M. D. Liberto, N. Goldman, I. Bloch, and M. Aidelsburger, Nat. Phys. **16**, 1058 (2020).
[13] N. Goldman, J. Dalibard, A. Dauphin, F. Gerbier, M. Lewenstein, P. Zoller, and I. B. Spielman, Proc. Natl. Acad. Sci. USA **110**, 6736 (2013).
[14] B. Song, L. Zhang, C. He, T. F. J. Poon, E. Hajiyev, S. Zhang, X.-J. Liu, and G.-B. Jo, Sci. Adv. **4**, eaao4748 (2018).
[15] C.-R. Yi, L. Zhang, L. Zhang, R.-H. Jiao, X.-C. Cheng, Z.-Y. Wang, X.-T. Xu, W. Sun, X.-J. Liu, S. Chen, and J.-W. Pan, Phys. Rev. Lett. **123**, 190603 (2019).
[16] T. Ozawa, H. M. Price, A. Amo, N. Goldman, M. Hafezi, L. Lu, M. C. Rechtsman, D. Schuster, J. Simon, O. Zilberberg, and I. Carusotto, Rev. Mod. Phys. **91**, 015006 (2019).
[17] T. Biesenthal, L. J. Maczewsky, Z. Yang, M. Kremer, M. Segev, A. Szameit, and M. Heinrich, Science **376**, 1114 (2022).
[18] M. S. Kirsch, Y. Zhang, M. Kremer, L. J. Maczewsky, S. K. Ivanov, Y. V. Kartashov, L. Torner, D. Bauer, A. Szameit, and M. Heinrich, Nat. Phys. **17**, 995 (2021).
[19] S. Mittal, S. Ganeshan, J. Fan, A. Vaezi, and M. Hafezi, Nat. Photonics **10**, 180 (2016).
[20] M. C. Rechtsman, J. M. Zeuner, Y. Plotnik, Y. Lumer, D. Podolsky, F. Dreisow, S. Nolte, M. Segev, and A. Szameit, Nature (London) **496**, 196 (2013).
[21] L. Lu, L. Fu, J. D. Joannopoulos, and M. Soljačić, Nat. Photonics **7**, 294 (2013).
[22] M. Hafezi, S. Mittal, J. Fan, A. Migdall, and J. M. Taylor, Nat. Photonics **7**, 1001 (2013).
[23] Y. Lumer, Y. Plotnik, M. C. Rechtsman, and M. Segev, Phys. Rev. Lett. **111**, 243905 (2013).

[24] A. B. Khanikaev, S. Hossein Mousavi, W.-K. Tse, M. Kargarian, A. H. MacDonald, and G. Shvets, Nat. Mater. **12**, 233 (2013).
[25] Z. Wang, Y. Chong, J. D. Joannopoulos, and M. Soljačić, Nature (London) **461**, 772 (2009).
[26] Y. Chen, Y. Yin, Z.-K. Lin, Z.-H. Zheng, Y. Liu, J. Li, J.-H. Jiang, and H. Chen, Phys. Rev. Lett. **129**, 154301 (2022).
[27] Q. Wang, H. Xue, B. Zhang, and Y. D. Chong, Phys. Rev. Lett. **124**, 243602 (2020).
[28] Y. Deng, W. A. Benalcazar, Z.-G. Chen, M. Oudich, G. Ma, and Y. Jing, Phys. Rev. Lett. **128**, 174301 (2022).
[29] S. Zheng, X. Man, Z.-L. Kong, Z.-K. Lin, G. Duan, N. Chen, D. Yu, J.-H. Jiang, and B. Xia, Sci. Bull. **67**, 2069 (2022).
[30] H. Xue, Y. Yang, F. Gao, Y. Chong, and B. Zhang, Nat. Mater. **18**, 108 (2019).
[31] Y. Qi, C. Qiu, M. Xiao, H. He, M. Ke, and Z. Liu, Phys. Rev. Lett. **124**, 206601 (2020).
[32] Z. Yang, F. Gao, X. Shi, X. Lin, Z. Gao, Y. Chong, and B. Zhang, Phys. Rev. Lett. **114**, 114301 (2015).
[33] C. He, X. Ni, H. Ge, X.-C. Sun, Y.-B. Chen, M.-H. Lu, X.-P. Liu, and Y.-F. Chen, Nat. Phys. **12**, 1124 (2016).
[34] J. Wang, S. Valligatla, Y. Yin, L. Schwarz, M. Medina-Sánchez, S. Baunack, C. H. Lee, R. Thomale, S. Li, V. M. Fomin, L. Ma, and O. G. Schmidt, Nat. Photonics **17**, 120 (2023).
[35] Y. Wu, M. Yan, Z.-K. Lin, H.-X. Wang, F. Li, and J.-H. Jiang, Sci. Bull. **66**, 1959 (2021).
[36] C.-W. Chen, R. Chaunsali, J. Christensen, G. Theocharis, and J. Yang, Commun. Mater. **2**, 62 (2021).
[37] S. D. Huber, Nat. Phys. **12**, 621 (2016).
[38] R. Süsstrunk and S. D. Huber, Science **349**, 47 (2015).
[39] S. Imhof, C. Berger, F. Bayer, J. Brehm, L. W. Molenkamp, T. Kiessling, F. Schindler, C. H. Lee, M. Greiter, T. Neupert, and R. Thomale, Nat. Phys. **14**, 925 (2018).
[40] C. H. Lee, S. Imhof, C. Berger, F. Bayer, J. Brehm, L. W. Molenkamp, T. Kiessling, and R. Thomale, Commun. Phys. **1**, 39 (2018).
[41] W. Zhang, F. Di, X. Zheng, H. Sun, and X. Zhang, Nat. Commun. **14**, 1083 (2023).
[42] W. Zhang, H. Yuan, H. Wang, F. Di, N. Sun, X. Zheng, H. Sun, and X. Zhang, Nat. Commun. **13**, 2392 (2022).
[43] J. Wu, Z. Wang, Y. Biao, F. Fei, S. Zhang, Z. Yin, Y. Hu, Z. Song, T. Wu, F. Song, and R. Yu, Nat. Electron. **5**, 635 (2022).
[44] W. Zhang, H. Yuan, N. Sun, H. Sun, and X. Zhang, Nat. Commun. **13**, 2937 (2022).
[45] T. Helbig, T. Hofmann, S. Imhof, M. Abdelghany, T. Kiessling, L. W. Molenkamp, C. H. Lee, A. Szameit, M. Greiter, and R. Thomale, Nat. Phys. **16**, 747 (2020).
[46] S. M. Rafi-Ul-Islam, Z. B. Siu, H. Sahin, and M. B. A. Jalil, Phys. Rev. B **106**, 245128 (2022).
[47] Y. Wang, L.-J. Lang, C. H. Lee, B. Zhang, and Y. D. Chong, Nat. Commun. **10**, 1102 (2019).
[48] Y. Hadad, J. C. Soric, A. B. Khanikaev, and A. Alú, Nat. Electron. **1**, 178 (2018).
[49] M. Ezawa, Phys. Rev. B **100**, 081401(R) (2019).
[50] D. Zou, T. Chen, W. He, J. Bao, C. H. Lee, H. Sun, and X. Zhang, Nat. Commun. **12**, 7201 (2021).
[51] C. Shang, S. Liu, R. Shao, P. Han, X. Zang, X. Zhang, K. N. Salama, W. Gao, C. H. Lee, R. Thomale, A. Manchon, S. Zhang, T. J. Cui, and U. Schwingenschlögl, Adv. Sci. **9**, 2202922 (2022).
[52] W. A. Benalcazar and A. Cerjan, Phys. Rev. B **101**, 161116(R) (2020).
[53] L. Qian, W. Zhang, H. Sun, and X. Zhang, Phys. Rev. Lett. **132**, 046601 (2024).